

This is an Open Access document downloaded from ORCA, Cardiff University's institutional repository: <https://orca.cardiff.ac.uk/id/eprint/156090/>

This is the author's version of a work that was submitted to / accepted for publication.

Citation for final published version:

Zhang, Man, Xu, Shaojun, Boubeche, Mebrouka, Decarolis, Donato, Huang, Yizhe, Liu, Biying, Gibson, Emma K., Li, Xin, Wang, Yuchen, Luo, Huixia, Catlow, C. Richard A. and Yan, Kai 2022. Designed TiS<sub>2</sub> nanosheets for efficient electrocatalytic reductive amination of biomass-derived furfurals. *Green Chemistry* 24 (24) , pp. 9570-9578. 10.1039/D2GC03234A

Publishers page: <http://dx.doi.org/10.1039/D2GC03234A>






Please note:

Changes made as a result of publishing processes such as copy-editing, formatting and page numbers may not be reflected in this version. For the definitive version of this publication, please refer to the published source. You are advised to consult the publisher's version if you wish to cite this paper.

This version is being made available in accordance with publisher policies. See <http://orca.cf.ac.uk/policies.html> for usage policies. Copyright and moral rights for publications made available in ORCA are retained by the copyright holders.



# Designed TiS<sub>2</sub> nanosheets for efficient electrocatalytic reductive amination of biomass-derived furfural†

Man Zhang,<sup>‡a</sup> Shaojun Xu,<sup>‡</sup>  <sup>b,c</sup> Mebrouka Boubeche,<sup>‡</sup>  <sup>d</sup> Donato Decarolis,<sup>b,c</sup> Yizhe Huang,<sup>a</sup> Biying Liu,<sup>a</sup> Emma K. Gibson,<sup>‡</sup>  <sup>c,e</sup> Xin Li,<sup>a</sup> Yuchen Wang,<sup>a</sup> Huixia Luo,<sup>‡</sup>  <sup>d</sup> C. Richard A. Catlow<sup>\*b,c,f</sup> and Kai Yan  <sup>\*a</sup>

Green and highly selective synthesis of organonitrogen chemicals (ONCs) using the renewable energy source biomass over noble-metal free solid catalysts under common room temperature and pressure conditions is still a major challenge. Here, we report a sustainable electrochemical method for selective synthesis of several valuable ONCs with high yields using biomass-derived furanic aldehydes over greenly fabricated TiS<sub>2</sub> nanosheets through a facile synthesis. Based on a range of characterization techniques including high-resolution transmission electron microscopy and X-ray absorption fine structure, a well-defined structure of the TiS<sub>2</sub> nanosheets (3.86 nm with 1T phase) was constructed. These as-prepared catalysts were applied to the electrochemical reductive amination (ERA) of three biomass-derived aldehydes, i.e. furfural (FF), 5-methylfurfural (MF) and 5-hydroxymethylfurfural (HMF), and exhibited superior performance whereby over 95% conversion of each furanic aldehyde and nearly perfect selectivity of ONCs were achieved. TiS<sub>2</sub> nanosheets, in particular, exhibited a marked ~2-fold increase in conversion (~49%) compared with the monometallic Ti electrode. Besides, the reaction kinetics and rational pathway were also studied. In addition, these exfoliated TiS<sub>2</sub> nanosheets maintained high durability over 6 h, providing a promising and versatile route for the sustainable upgrading of biomass-derived sources.

## Introduction

Organonitrogen chemicals (ONCs) are crucial platform chemicals for manufacturing dyes, pharmaceuticals, drug intermediates, surfactants and agrochemicals.<sup>1–4</sup> It was reported that over 80% of the top 200 pharmaceuticals were derived from amines in 2020.<sup>5,6</sup> The conventional synthesis of ONCs is mainly from alkyl halides, nitro complexes, or nitriles, with

which many by-products and waste are associated.<sup>7–9</sup> The direct reductive amination of aldehydes with ammonia or organic amines has been envisioned as an alternative for ONC production.<sup>10,11</sup> In particular, aldehydes could be readily produced from renewable biomass resources and water is the sole by-product of the reaction, thus reducing the carbon footprint.<sup>12,13</sup>

The selective synthesis of ONCs remains a big challenge due to the easily occurring side reactions.<sup>14–20</sup> Taking furanic aldehydes as an example, the amination reaction involves a complicated pathway as depicted in Scheme 1. The target ONC could be selectively generated from the condensation of furanic aldehydes (a) with ethanolamine through C–N coupling and then via the hydrogenation of the primary imine to the ONC.<sup>11</sup> As shown in Scheme 1, when the main reaction of the target ONC (c) took place, the direct hydrogenation and/or hydrogenolysis of furanic aldehydes to alcohols (d) and furans (e) would compete with the reaction pathway of the ONC. The progress of robust catalysts and the catalytic system for the process are of great importance for the synthesis of ONC.<sup>21–24</sup>

So far, the most widely used catalysts contain noble metals (e.g. Ru, Pt, Pd, Rh, and Au) in traditional synthesis.<sup>25–30</sup> Gross et al. reported the efficiency of reductive amination of benzaldehyde to benzylamine on the homogeneous Rh catalyst at

<sup>a</sup>School of Environmental Science and Engineering, Guangdong Provincial Key Laboratory of Environmental Pollution Control and Remediation Technology, Sun Yat-sen University, Guangzhou 510275, China. E-mail: yank9@mail.sysu.edu.cn

<sup>b</sup>School of Chemistry, Cardiff University, Main Building, Park Place, Cardiff, CF10 3AT, UK. E-mail: c.r.a.catlow@ucl.ac.uk

<sup>c</sup>UK Catalysis Hub, Research Complex at Harwell, Rutherford Appleton Laboratory, Harwell, OX11 0FA, UK

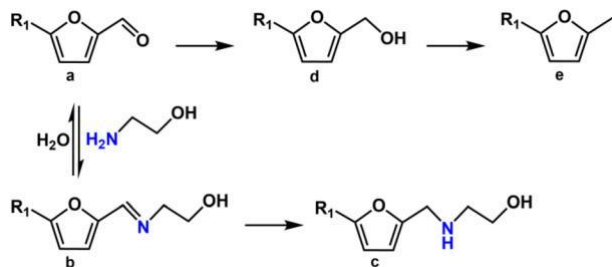
<sup>d</sup>School of Materials Science and Engineering and Key Lab Polymer Composite & Functional Materials, Sun Yat-sen University, Guangzhou, 510275, China

<sup>e</sup>School of Chemistry, Joseph Black Building, University of Glasgow, Glasgow G12 8QQ, UK

<sup>f</sup>Department of Chemistry, University College London, 20 Gordon Street, London, WC1H 0AJ, UK

†Electronic supplementary information (ESI) available. See DOI: <https://doi.org/10.1039/d2gc03234a>

‡These authors contributed equally to this work.



Scheme 1 Reaction process for the reductive amination of furanic aldehydes. The target product organonitrogen chemicals (ONC, c) from furanic aldehydes (a) amination is obtained, wherein a series of side reactions (a–e) may involve. (R<sub>1</sub> is hydrogen, methyl-, ethyl-, and hydroxymethyl).

135 °C and with 6.5 MPa reducing gas.<sup>31</sup> Mei et al. considered the electro-synthesis method at 70 °C.<sup>32</sup> They discovered that C–H bond amination in organopalladium intermediates produced an ONC product with 82% yield. However, these described catalysts exhibited a fair amount of amine selectivity. Some metal electrodes such as Pt, Cu, Ag etc. exhibited high selectivity (nearing 100%) through electrochemical reduction avoiding high temperature.<sup>33</sup> The enhanced selectivity largely depended on the metal's specific active capacity.<sup>34,35</sup> It is highly desirable, therefore, to develop improved protocols for synthesizing ONCs using an inexpensive catalyst.

Low-cost transition metal dichalcogenides,<sup>36</sup> which are a new family of 2D nanosheets, are promising candidates due to their wide operational voltage, long cycle-life, high surface ion diffusivities, and ultrafast charge/discharge capabilities.<sup>37–43</sup> Recent efforts have been made to utilize transition metal dichalcogenides (e.g., MoS<sub>2</sub> and TaS<sub>2</sub>) for the hydrogen evolution reaction.<sup>34,44–47</sup> However, few studies have utilized tran-

sition metal dichalcogenide catalysts for the sustainable synthesis of ONCs from biomass-derived furanic aldehydes.

Here, we documented a sustainable method for the electrochemical reductive amination (ERA) of various furanic aldehydes over TiS<sub>2</sub> nanosheets at room temperature and pressure (as illustrated in Fig. 1). TiS<sub>2</sub> nanosheets were firstly fabricated through solid-state synthesis without the use of organic solvents, and then exfoliated using 10 mL of isopropanol. The physical properties of the obtained TiS<sub>2</sub> were then characterized by high-resolution transmission electron microscopy (HR-TEM), electron paramagnetic resonance (EPR), and X-ray absorption fine structure (XAFS) analysis. These as-prepared TiS<sub>2</sub> nanosheets exhibited superior performance for the ERA of three biomass-derived compounds: furfural (FF), 5-methyl-furfural (MF) and 5-hydroxymethylfurfural (HMF) in 0.7 M ethanolamine. Over 95% conversion of furanic aldehydes, nearing perfect selectivity of the ONC, and good turnover number (TON) and high stability were achieved. The results showed a marked ~2-fold improvement of furfural conversion in comparison with the Ti electrode (<50%). These controllably synthesized laminate TiS<sub>2</sub> nanosheets offer the following benefits: (i) thin nanosheets, supplying sufficient surface active centres, (ii) a large electrochemically active surface area (ECSA), a small Tafel slope and faster kinetics, (iii) a high concentration of sulfur vacancies, enhancing the adsorption of reactants, and (iv) high stability and good durability over 6 h.

## Results and discussion

### Characterization of laminate TiS<sub>2</sub> nanosheets

The morphology and surface textural properties of the as-synthesized laminate TiS<sub>2</sub> nanosheets were firstly determined by

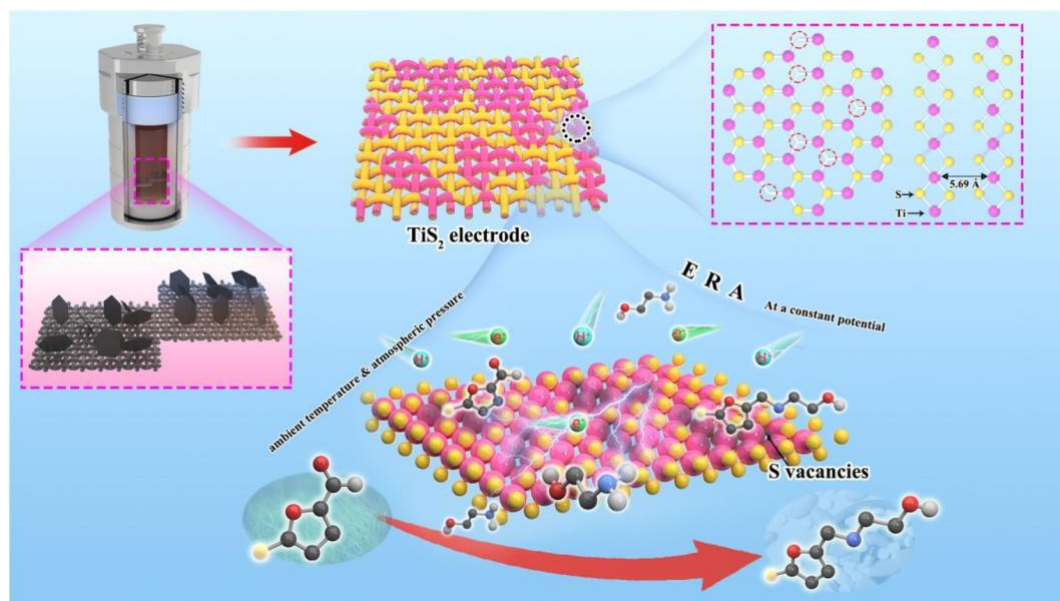


Fig. 1 Schematic view of the controllable synthesis of TiS<sub>2</sub> nanosheets electrode and the ERA reaction.



transmission electron microscopy (TEM), as detailed in the ESI.† TEM images (Fig. S1a and b†) showed a typical layered structure of transition metal dichalcogenides. The high-resolution HR-TEM image (Fig. 2a) of TiS<sub>2</sub> showed the characteristic lattice fringes of the (001) plane with the lattice spacing of 0.569 nm. In addition, the ring and spot in the selected area electron diffraction (SAED) confirmed the structure of TiS<sub>2</sub>. As shown in Fig. 2b, the well-defined rings could be indexed into the (001), (101), (102), (110), (103), (004) and (202) planes of TiS<sub>2</sub>. Moreover, the interplanar spacing of 0.569 and 0.262 nm were measured in an enlarged view of Fig. 2c corresponding to the (001) and (101) planes of TiS<sub>2</sub>. In addition, the HR-TEM image in Fig. S2a† showed that TiS<sub>2</sub> is located on the ⟨100⟩ zone axis, as per the schematic view of the TiS<sub>2</sub> crystal lattice (Fig. S2b†). The energy-dispersive X-ray spectroscopy (EDS) analysis showed the uniform distribution of Ti and S as displayed in Fig. 2d–f. Moreover, the atomic force microscopy (AFM) analysis (Fig. 2g) showed that laminate TiS<sub>2</sub> nanosheets had an average thickness of 3.86 ± 0.17 nm (Fig. 2h). As shown in Fig. S3,† the height profile had a mean value of 3.86 nm, indicating that laminate TiS<sub>2</sub> nanosheets comprised 6–8 layers.

The as-synthesized TiS<sub>2</sub> was further characterized by powder X-ray diffraction (XRD), as detailed in the ESI.† In Fig. S4a,† the characteristic signals in the diffractogram of TiS<sub>2</sub>

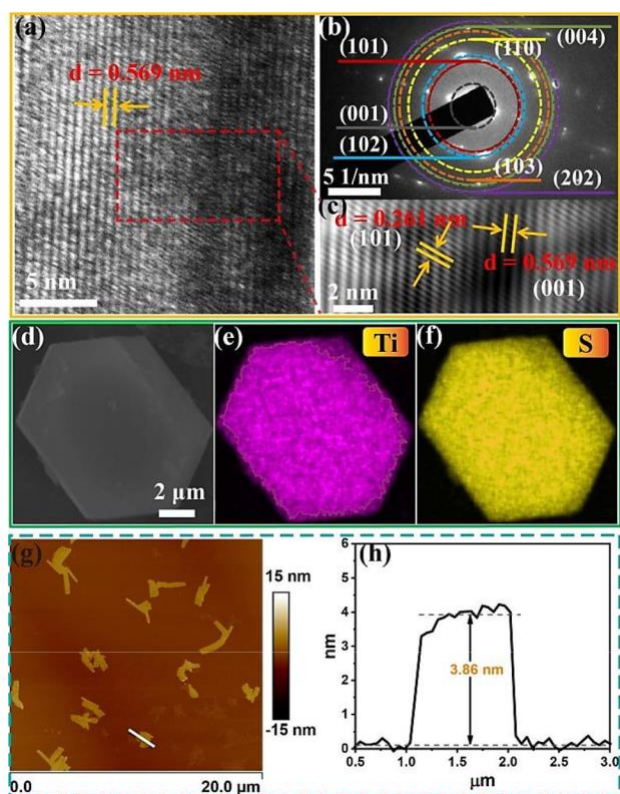


Fig. 2 (a) HR-TEM image, (b) SAED pattern, (c) corresponding inverse fast Fourier transform (FFT) image of areas in red frame in (a), and (d, e and f) elemental mapping of the as-synthesized TiS<sub>2</sub>. AFM image (g) and height profile (h) of TiS<sub>2</sub>.

were well-indexed to a hexagonal structure (JCPDS Card No. 15-0853). The Bragg positions correspond with the P 3m1 (No. 164) space group ( $a = 3.405 \text{ \AA}$ ,  $b = 3.405 \text{ \AA}$ , and  $c = 5.691 \text{ \AA}$ ).<sup>48</sup> In addition, Raman spectroscopy was performed to investigate the surface bond of TiS<sub>2</sub> as an effective tool to study defects. In general, TiS<sub>2</sub> had two Raman active modes: in-plane vibrational mode ( $E_g$ ) and out-of-plane mode ( $A_{1g}$ ).<sup>49,50</sup> However, the as-synthesized TiS<sub>2</sub> showed two main peaks at 228  $\text{cm}^{-1}$  and 330  $\text{cm}^{-1}$  (assigned to  $E_g$  and  $A_{1g}$ ), but also a “shoulder peak” at 382  $\text{cm}^{-1}$  (Fig. S4b†). The “shoulder peak” suggest that the stiffened phonon modes are responsible for the temperature-dependent scattering because of the appearance of sulfur vacancies in the TiS<sub>2</sub> material.<sup>51,52</sup> The schematic structure of TiS<sub>2</sub> is depicted in Fig. S4b† with the Ti atom layer located in the middle of the two S atom layers with which it formed covalent bonds. After that, the van der Waals interactions held the S–Ti–S layers together. TiS<sub>2</sub> material was in the 1T phase based on the stacking ordering of S–Ti–S layers along the c axis (vertical direction).<sup>53</sup> This unique two-dimensional spacing structure was beneficial for allowing the ready diffusion and transport of platform molecules (e.g., FF, MF and HMF).

To obtain an understanding of surface defects, EPR was executed to study the spin states of TiS<sub>2</sub> as detailed in the ESI.† The results are shown in Fig. 3a. Laminate TiS<sub>2</sub> nanosheets revealed a strong EPR peak at  $g = 2.003$ , which corresponds to more exposed active centres due to sulfur vacancies.<sup>54,55</sup> Furthermore, the chemical status of the Ti–S bond and the local structure of the metal cations were investigated by the analysis of the X-ray absorption fine structure (XAFS) collected at the Ti K-edge (Fig. 3b). The X-ray absorption near-edge structure (XANES) spectra of the as-prepared TiS<sub>2</sub> compare well with the standard TiS<sub>2</sub> reference. A reasonable fit of the Fourier transform of the  $k^2$  weighted XAFS data (Fig. 3c and d) was obtained using the Ti–S scattering paths at  $2.43 \pm 0.02 \text{ \AA}$  for the as-synthesized TiS<sub>2</sub>. This distance was consistent with that obtained for the standard TiS<sub>2</sub> reference at  $2.40 \pm 0.02 \text{ \AA}$  (Table S1†). For the intensity of the feature at low R in Fig. 3c, the as-synthesized TiS<sub>2</sub> was lower than that of a TiS<sub>2</sub> reference material, in agreement with the XAFS fit of the 1<sup>st</sup> shell Ti–S path giving coordination numbers of  $(3.1 \pm 0.8)$  and  $(4 \pm 1)$  for as-synthesized TiS<sub>2</sub> and standard TiS<sub>2</sub> reference, respectively (Table S1†). That implied the presence of sulfur vacancies, and exposing more metal active sites. In addition, the wavelet transform (WT) analysis of Ti XAFS oscillations was conducted. For the WT contour plot of TiS<sub>2</sub> (Fig. 3e and f), one intensity maximum at near  $\sim 4 \text{ \AA}^{-1}$  was observed, which was assigned to the Ti–S contribution.

### Electrochemical reductive amination (ERA)

To evaluate these prepared catalysts, ERA reactions of furanic aldehydes over a TiS<sub>2</sub> electrode were firstly examined by scanning linear sweep voltammetry (LSV) curves in a three-electrode system. The change of cathodic current was obtained in ethanolamine electrolyte with and without 5 mM furfural (FF) is shown in Fig. 4a. In the absence of FF, the cathode current

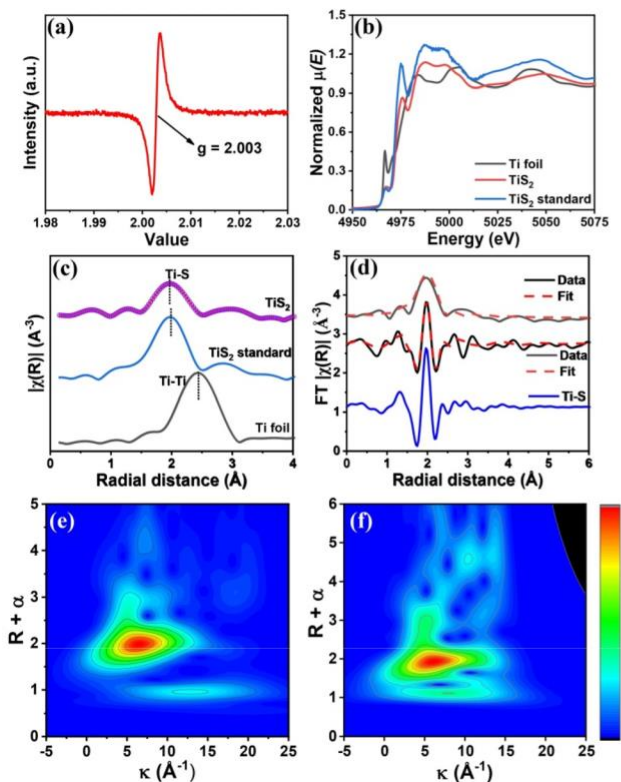


Fig. 3 (a) EPR spectrum of  $\text{TiS}_2$ , (b) normalized Ti K-edge XANES spectra of as-synthesized  $\text{TiS}_2$  and standard XANES spectra of Ti foil and  $\text{TiS}_2$  recorded as references, (c) non-phase corrected Fourier-transformed  $k^2$  weighted XAFS of as-synthesized  $\text{TiS}_2$  and the standard  $\text{TiS}_2$  as references, (d) stacked plots of the magnitude (top) and imaginary (bottom) non-phase corrected Fourier-transformed Ti K-edge XAFS. XAFS wavelet transforms spectra of (e) commercial  $\text{TiS}_2$  and (f) the as-synthesized  $\text{TiS}_2$ .

was attributed to the reduction of water to generate  $\text{H}_2$ .<sup>33</sup> After adding 5 mM FF into ethanolamine, the onset current increases, and a positive 160 mV shift in the onset potential was observed. Also, before water reduction, there was a well-defined diffusion-limited reduction peak for aldimine, which suggested that the ERA of FF was more favoured over water reduction on the  $\text{TiS}_2$  nanosheets. Although there was no obvious onset shift in the LSV curves for the  $\text{TiS}_2$  electrode with and without 5-methylfurfural (MF), the current density gradually increased at the implemented potential range of  $E < -0.4$  V vs. RHE ( $V_{\text{RHE}}$ ) by eqn (S1).<sup>†</sup> These results indicated that the aldimine reduction had slow dynamics equivalent to water reduction in ethanolamine containing 5 mM MF on the  $\text{TiS}_2$  nanosheet electrode. Meanwhile, blank carbon fibre paper and Ti foil as working electrodes for ERA were compared and considered. LSV curves showed the poor current efficiency in Fig. S5<sup>†</sup>. The result indicated that  $\text{TiS}_2$  showed high-efficiency metal sites for ERA due to the sulfur vacancies. Additionally, the Tafel slope was given in Fig. 4b, exhibiting the fast dynamic interaction of ERA with and without furanic aldehydes. The Tafel slope ( $300 \text{ mV dec}^{-1}$ ) after adding FF was smaller than that of pure water reduction without FF ( $375 \text{ mV}$

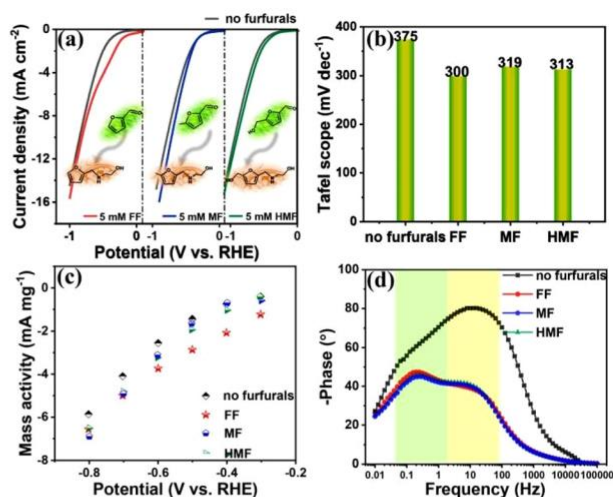


Fig. 4 (a) LSV curves of  $\text{TiS}_2$  electrode in 0.7 M ethanolamine electro-lyte (no furfurals) and ethanolamine containing 5 mM FF at scan rate  $5 \text{ mV s}^{-1}$ . Likewise, LSV curves in 5 mM MF and 5 mM HMF. (b) Corresponding Tafel slope. (c) Mass activity of  $\text{TiS}_2$  electrode in diverse electrolytes at different applied potentials. (d) Bode plots in ethanol-amine electrolyte and with FF, MF, HMF, respectively.

$\text{dec}^{-1}$ ), suggesting the accelerated dynamics of the ERA reaction. In Fig. S6,<sup>†</sup> the furfural adsorption peaks are obvious in the LSV curves at a slow scan rate of  $2 \text{ mV s}^{-1}$ .

The electrochemically active surface area (ECSA) for the three furanic aldehydes was also studied to understand the effect of the catalysts' surface adsorption capacity on the electrochemical reductive amination reactions (Fig. S7a–7c<sup>†</sup>). The electrochemical double-layer capacitance (Fig. S7d<sup>†</sup>) values via eqn (S2)<sup>†</sup> were 0.13, 0.11, and 0.12  $\text{mF cm}^{-2}$  in FF, MF, and HMF, respectively. Furthermore, laminate  $\text{TiS}_2$  nanosheets yielded an ECSA (eqn (S3)<sup>†</sup>) of  $3.25 \text{ cm}^2$  within FF,  $2.75 \text{ cm}^2$  in MF and  $3.00 \text{ cm}^2$  in HMF. After the ERA, the ECSA values were  $3.25$ ,  $2.72$ , and  $2.95 \text{ cm}^2$ , respectively. These further confirmed that laminate  $\text{TiS}_2$  nanosheets exhibited a large activity area in the ERA.

In addition, the mass activity was estimated using eqn (S4)<sup>†</sup> as shown in Fig. 4c. It is noted that the mass activity in FF5 was superior to those in MF and HMF at the applied potential of  $-0.3$  to  $-0.6 V_{\text{RHE}}$ . In particular, at the applied potential of  $-0.3 V_{\text{RHE}}$ , the mass activity of  $1.23 \text{ mA mg}^{-1}$  in FF was 3.0 and 2.1 times greater than those in MF ( $0.41 \text{ mA mg}^{-1}$ ) and HMF ( $0.59 \text{ mA mg}^{-1}$ ). However, at  $-0.7$  and  $-0.8 V_{\text{RHE}}$ , the mass activity was approximately equal for the different furanic aldehydes, implying the low current efficiency at a high applied potential. Besides, the bold plots in Fig. 4d showed the ridge peaks in ethanolamine containing 5 mM FF (or MF, or HMF) at a low frequency interface, compared with only one peak curve in the curve for pure ethanolamine. These results indicated that ERA reactions had a higher priority and were efficient with the addition of FF (or MF, or HMF). The low overpotential, small Tafel slope and large ECSA suggested that the  $\text{TiS}_2$  nanosheet electrode exhibited a high ERA activity.

The turnover frequency (TOF, Fig. S8a†) for the three reductive aminations over TiS<sub>2</sub> nanosheets at -500 mV was computed using eqn (S5)† to highlight the intrinsic reduction activity in detail. In particular, the computed TOF value of 0.407 s<sup>-1</sup> for 5 mM FF was significantly greater (pure water oxidation of 0.205 s<sup>-1</sup>). These results suggested that the TOF of FF was nearly 2 times greater than that of no furfurals, further indicating that the ERA is the dominant reaction.

The effect of applied potential on the reduction of three furanic aldehydes over TiS<sub>2</sub> nanosheets was shown in Fig. S8b† and Table 1. The average current density of 1.45 mA cm<sup>-2</sup> in FF was much higher than the value of 0.82 mA cm<sup>-2</sup> in MF and 1.24 mA cm<sup>-2</sup> in HMF at the potential of -0.4 V<sub>RHE</sub>. The concentration of furan aldehydes decreased gradually over 6 h for each of the products produced from the reductive amination, with the respective products having HPLC retention time of 5.4 min (FF), 8.2 min (MF) and 4.8 min (HMF) in Fig. S9.† To identify reaction intermediates, the standard curves of FF, MF and HMF (Fig. S10†) and ultra-performance liquid chromatography /tandem mass spectrometry (UPLC-MS/MS) were carried out, as described in the Experimental section. In the MS spectrum (Fig. S11a†), the mass-to-charge ratio (m/z) of 141.16 was confirmed as that of the amine product 5-(ethanolaminemethyl) furan (EMF) from FF. The m/z of 121.02 (Fig. S11b†) was from the detachment of a H<sub>2</sub>O molecule from EMF. Similarly, the m/z of 155.19 (Fig. S11c†) and 171.19 (Fig. S11d†) were assigned to 2-methyl-5-(ethanolamine methyl) furan (MEMF) and 2-hydroxymethyl-5-(ethanolamine methyl) furan (HEMF), respectively. In addition, the conversion rates of the three amination reactions over time at different potentials were further calculated and are shown in Table 1 and Fig. S12.† For FF (Fig. S12a†), 78% conversion efficiency was reached at -0.6 V<sub>RHE</sub> by eqn (S6).† Besides, carbon fiber

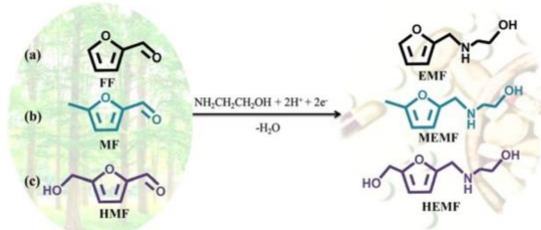
paper was used, which had limited reduction amination efficiency with a poor yield of 15%. In the absence of a catalyst, the reductive amination was quite unsatisfactory. FE (43.7%, eqn (S8)†) was obviously enhanced at a potential of -0.6 V<sub>RHE</sub> as shown in Fig. S13,† which was much better than the value of 26.1% at -0.4 V<sub>RHE</sub> and 18.5% at -0.8 V<sub>RHE</sub>. A similar trend was also observed in the case of HMF. The selectivity of ald-imine reduction was approximately 100% over TiS<sub>2</sub> nanosheets from eqn (S7)† and TON was then used to calculate the effective utilization rate of catalysts from eqn (S9),† which was defined as mole of substrate reacted per mole of catalyst. The TON values for the FF reductive amination reaction reached 357 at -0.6 V<sub>RHE</sub>, while a TON of over 300 for MF and HMF for ERA was reached. To compare the viability of ERA, ethanedia-mine as a nitrogen source was used to investigate the products. As shown in Fig. S14,† all yields of ONC were over 85%.

In addition, the mass of product per mass of active surface area (MASA) of the electrode was also calculated using eqn S10.† As shown in Table 1, the MASA in 5 mM FF electrolyte is 58.6 mg cm<sup>-2</sup> for EMF at a low potential, 32.9 mg cm<sup>-2</sup> for MF and 38.9 mg cm<sup>-2</sup> for HMF, indicating the high-efficiency of ERA within the FF electrolyte and loss (<0.1 mg) of the catalyst during the ERA process was negligible. When compared to the electrochemical and traditional, j, TOF, MASA, and TON were used to construct a comprehensive assessment system for ERA.

#### Catalyst stability and potential pathway

Catalyst stability is a crucial criterion for a viable process. The typical crystal planes of the catalyst post the reaction (Fig. S15†) corresponded well with the specific phase of the fresh TiS<sub>2</sub> nanosheets.<sup>56</sup> During 6 h of ERA, the current curve was stationary at -0.8 V<sub>RHE</sub> in Fig. S16.† Raman spectra (Fig. S17†) also confirmed the high stability of TiS<sub>2</sub> with E<sub>g</sub>

Table 1 Results obtained from the ERA at various potentials



| Furanic aldehydes | Potential applied (V <sub>RHE</sub> ) | Average current (mA cm <sup>-2</sup> ) | Conversion (%) | Selectivity (%) | FE (%) | MASA (mg cm <sup>-2</sup> ) | TON |
|-------------------|---------------------------------------|--|----------------|-----------------|--------|-----------------------------|-----|
| FF                | -0.4                                  | 1.45                                   | 27             | >99             | 33.3   | 58.6                        | 101 |
|                   | -0.6                                  | 4.21                                   | 90             | >99             | 38.2   | 195.5                       | 338 |
|                   | -0.8                                  | 10.52                                  | 95             | >99             | 16.1   | 206.9                       | 357 |
| MF                | -0.4                                  | 0.82                                   | 12             | >99             | 26.1   | 32.9                        | 42  |
|                   | -0.6                                  | 2.94                                   | 72             | >99             | 43.7   | 197.5                       | 252 |
|                   | -0.8                                  | 8.30                                   | 86             | >99             | 18.5   | 235.9                       | 301 |
| HMF               | -0.4                                  | 1.24                                   | 14             | >99             | 20.2   | 39.9                        | 49  |
|                   | -0.6                                  | 4.57                                   | 88             | >99             | 34.4   | 251.1                       | 308 |
|                   | -0.8                                  | 8.90                                   | 91             | >99             | 18.3   | 259.6                       | 318 |

Conversion, selectivity, and FE were calculated using eqn (S6)–(S10) (ESI†).



and  $A_{1g}$  modes at  $228\text{ cm}^{-1}$  and  $330\text{ cm}^{-1}$ , respectively. XPS spectra were subsequently used to compare the structural changes of the pristine and spent  $\text{TiS}_2$  electrode. After under-going the ERA, the two peaks at the binding energies of 161.1 and 162.8 eV in the high-resolution S 2p spectrum correspond to Ti-S and S-S covalent bonds in Fig. S18a and S18b.†<sup>57–59</sup> In comparison with the fresh electrode, no apparent morphological change is seen in the SEM images (Fig. S19†). The HR-TEM image (Fig. S18c†) of  $\text{TiS}_2$  nanosheets clearly shows a lattice distance of 0.285 nm, corresponding to the (002) crystal face. Fig. S18d† displays the SAED pattern with typical planes of  $\text{TiS}_2$ . Furthermore, the catalytic performance (Fig. S18e and S20†) for ERA was executed using the recycled  $\text{TiS}_2$  nanosheets. Over five runs of FF aminations,  $\text{TiS}_2$  kept over 90% FF conversion with very little mass loss of the electrode and over 95% selectivity for EMF. Even after 30 h, only 5% decay was found in the case of MF and HMF.

In order to give an in-depth insight into the ERA reaction, the ERA catalytic process over laminate  $\text{TiS}_2$  nanosheets was studied by in situ diffuse reflectance infrared Fourier transform spectroscopy (DRIFTS), as the methodology detailed in ESI.† The results of DRIFTS measurement as shown in Fig. 5a show that the (C–H) stretching vibrations of fresh FF were observed at  $2810$  and  $2848\text{ cm}^{-1}$ , compared to the (C–H) stretching vibrations of the amine containing products at  $2920$  and  $2848\text{ cm}^{-1}$ . This result allowed the reaction sequence to be followed via DRIFTS.<sup>60,61</sup> For the spectra of FF and ethanolamine solution in Fig. S21,† there were two new peaks at  $1631$  and  $1660\text{ cm}^{-1}$ , ascribed to the intermediate in the mixed solution. As reaction time increased, the stretching vibration of the –N–

H with C–N species from the product of EMF was found in the  $3350\text{ cm}^{-1}$  region, along with the presence of several newly formed bands ( $1557\text{ cm}^{-1}$  and  $1508\text{ cm}^{-1}$ ) ascribed to the –C–N stretching vibration of EMF.<sup>24,62</sup> In addition, a right shift from  $1276$  and  $1250\text{ cm}^{-1}$  of FF to  $1257$  and  $1243\text{ cm}^{-1}$  for ERA was ascribed to  $\delta(\text{C–H})$  of the –CVO bond, which is ascribed to FF molecular adsorption on the surface of vacancy-rich  $\text{TiS}_2$ .<sup>63,64</sup> After the electrochemical reductive amination reaction, a peak at  $2591\text{ cm}^{-1}$  was observed. This peak was attributed to the S–H···OVC interaction between organic molecules and the vacancy-rich  $\text{TiS}_2$  nanosheets.<sup>65,66</sup> Therefore, the ERA reaction with FF reacting over the sulfur vacancy-rich  $\text{TiS}_2$  nanosheets is proposed in Fig. 5b. In the amination reaction, laminate  $\text{TiS}_2$  nanosheets have a larger ECSA and a fast reaction kinetics resulting in a left shift of the LSV curve with a high TOF value for 0.7 M ethanolamine and FF electrolyte. Sulfur vacancies on the thin surface can adsorb more reactants and the layered structure of  $\text{TiS}_2$  nanosheets would expose more active sites. In the process of the ERA, the aldehyde group was firstly dehydrated with ethanolamine in a nucleophilic reaction to produce an imine. Subsequently, the imine could be quickly reduced to obtain aminofurans through in situ generated  $\text{H}^+$  from  $\text{H}_2\text{O}$  accompanied by an electron source. The imine was then hydrogenated by breaking the CvN double bond after gaining an electron. By applying the suitable voltage to generate EMF, MEMF, and HEMF, the direct ERA was further increased.

## Conclusions

Laminate 1T- $\text{TiS}_2$  nanosheets with a thickness of 3.86 nm were successfully fabricated and exhibited reliable performance (over 95% conversion with nearly satisfactory selectivity) for the highly selective synthesis of various ONCs using biomass-derived furanic aldehydes (e.g. FF, MF, and HMF) at ambient temperature and atmospheric pressure. When 5 mM FF was introduced, the onset potential dramatically shifted toward the positive direction of water reduction. A TOF value of  $0.407\text{ s}^{-1}$  at  $-0.5\text{ V}_{\text{RHE}}$  was reached, which was much larger than those within ethanolamine electrolytes of  $0.205\text{ s}^{-1}$  with MF and  $0.287\text{ s}^{-1}$  using HMF. The  $\text{TiS}_2$  nanosheets exhibited the highest performance and fastest kinetics of ERA using the FF substrate. These were attributed to the largest electrochemically active surface area laminate of  $3.25\text{ cm}^2$  in 5 mM FF, compared with  $2.75\text{ cm}^2$  in 5 mM MF and  $3.00\text{ cm}^2$  in 5 mM HMF.

Through electrochemical CVO activation, we have uncovered the first ERA of C–N that enables the use of sustainable electricity leading to EMF, MEMF and HEMF. The notable features of this work are attributed to more active sites available on the thin nanosheets. Importantly, the hydrogen source was water avoiding the use of chemical reducing agents and ERA achieved the high selectivity of the ONC product at ambient temperature/pressure. Over 95% conversion and nearly 100% selectivity with a low overpotential were achieved. Besides, the laminate 1T- $\text{TiS}_2$  nanosheets maintained a stable structure

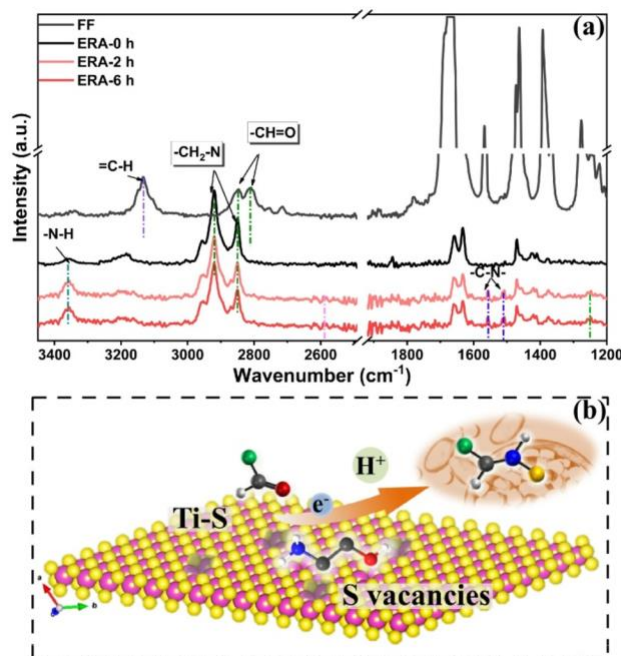


Fig. 5 (a) In situ diffuse reflectance infrared Fourier transform spectroscopy (DRIFTS) of FF and solution during ERA. (b) The proposed reductive amination pathway of furanic aldehydes over  $\text{TiS}_2$ .

and high durability in the ERA process. This work provides an eco-friendly and efficient alternative for the synthesis of various ONCs from biorefineries.

## Experimental section

### Controllable synthesis of laminate TiS<sub>2</sub> nanosheets

Purities and chemical sources used in this work are described in the ESI (ESI 1.1†). TiS<sub>2</sub> nanosheets were facilely and control-lably synthesized by the direct reaction of Ti powder and sulfur powder. The obtained laminated TiS<sub>2</sub> catalysts were further treated by quenching with a solution of ice and water. After that, the exfoliated TiS<sub>2</sub> nanosheets were obtained in isopro-panol (20 mL) using ultrasonic treatment. The general pro-cedure is illustrated in Fig. 1 and more details are indicated in the controllable synthesis of TiS<sub>2</sub> nanosheets (ESI†).

### Electrochemical synthesis of aminofurans

20 mL of 0.7 M ethanolamine solution (see the ESI†) was transferred into a four-necked flask with a volume of 25 mL. The electrochemical testing was conducted using Autolab M204 purchased from Metrohm in a typical three-electrode system with Ar-saturation for the reductive amination. The working electrode (WE) was fabricated by coating TiS<sub>2</sub> nanosheets on carbon fibre paper. Pt wire ( $\Phi = 1$  mm, 4 cm of length, Shanghai CH Instruments Ins, China) as the counter electrode (CE), and a Hg|HgO (Gaoss Union, single salt bridge) as the reference electrode (RE) was used for all electrochemical reduc-tive amination (ERA) reactions at room temperature and pressure. The acquired potential was standardized to the reversible hydrogen electrode (RHE) according to eqn (S1) (see ESI†). The scanning linear sweep voltammetry (LSV) curves were investigated at the applied potential range of 0.1 to  $-1.0 V_{RHE}$  at a scan rate of  $5 \text{ mV s}^{-1}$ . The ERA reactions were executed in 0.7 M ethanolamine with and without the different furanic aldehydes of 5 mM FF, MF, and HMF at a constant applied potential with a stirring rate of 600 rpm in one com-partment. The IR value was compensated for the standing voltage drop between the WE and RE via Nova Software in all the electrochemical tests.

### Analysis of products

To analyse quantitatively the concentration of the reactant in the ERA, 100  $\mu\text{L}$  of the solution was taken from the homo-geneous electrolyte solution during chronoamperometry at  $-0.4$ ,  $-0.6$  and  $-0.8 V_{RHE}$ . The conversion of FF, MF, and HMF was evaluated by high-performance liquid chromatography (HPLC, mode: Shimadzu Prominence LC-20A), with a Shimadzu column (C 18, size:  $5 \mu\text{m}$ ,  $4.6 \times 150$  mm) and an ultraviolet-visible detector (265 nm). A mixed mobile phase 5 mM ammonium formate aqueous (70 vol%) and methanol (30 vol%) was used to detect the reaction liquid at a flow rate of  $1.0 \text{ mL min}^{-1}$ . The injection volume was 10  $\mu\text{L}$ . The species and selectivity of products using multiple-reaction monitoring mode were investigated through ultra-performance liquid

chromatography in conjunction with triple-quadrupole tandem mass spectrometry (UPLC-MS/MS). UPLC-MS/MS assay using negative ion mode was implemented by a Waters ACQUITY UPLC CSH™ C18 ( $2.1 \text{ mm} \times 50 \text{ mm}$  column,  $1.7 \mu\text{m}$ ) with the mixed mobile phase including acetonitrile and 0.1% methanoic acid at  $0.3 \text{ mL min}^{-1}$  by gradient elution. For specific details, acetonitrile dosage was 10% in 0–1 min, 90% in 1.1–3 min, and 10% in 12.1–13 min.

### Ex situ X-ray absorption spectroscopy (XAS) measurements

The X-ray absorption spectroscopy (XAS) measurements were carried out at the Ti K-edge (4966 eV) on the B18 beamline at the Diamond Light Source, Didcot, UK. Measurements were carried out in transmission mode utilizing a QEXAFS device with fast-scanning Si (111) double crystal monochromators for the Ti k-edge. The data processing was performed using IFEFFIT with the Demeter package (Athena and Artemis).<sup>67</sup> Fitting parameters:  $S_0^2 = 0.707$  calculated from the foil, fit range  $3 < k(\text{\AA}^{-2}) < 10.5$ ,  $1.4 < R(\text{\AA}) < 2.5$ ; and number of inde-pendent points = 5.1.

## Author contributions

M. Z.: Electrochemical reaction operation. S. X.: Sample characterization and manuscript revision. M. Z., E. K. G., S. X., M. B. and D. D.: Data curation. Y. H.: Synthesis of material. B. L.: Writing the experiment part. X. L. and Y. W.: Sorting out the ESI.† S. X., C. R. A. C., H. L. and K. Y.: Writing – review & editing. C. R. A. C. and K. Y.: Supervision.

## Conflicts of interest

There are no conflicts to declare.

## Acknowledgements

This work was supported by the National Key R&D Program of China (2020YFC1807600), National Natural Science Foundation of China (11922415 and 22078374), National Ten Thousand Talent Plan, Guangdong Basic and Applied Basic Research Foundation (2019B1515120058), the Pearl River Scholarship Program of Guangdong Province Universities and Colleges (20191001), and the Scientific and Technological Planning Project of Guangzhou, China (202206010145). We also thank Diamond Light Source for access to the Beamlines B18 and also the Diamond Light Source beamline staff and the UK catalysis Hub Block Allocation Group (BAG) Programme Mode Application, in particular Dr Veronica Celorrio and Dr June Callison, for provision of beamtime at B18 (Experiment SP19850-6) for collection of the data and the initial discussion. The UK Catalysis Hub is kindly thanked for resources and support provided via our membership of the UK Catalysis Hub Consortium and funded by the EPSRC grant:



## References

- 1 T. Senthamarai, K. Murugesan, J. Schneidewind, N. V. Kalevaru, W. Baumann, H. Neumann, P. C. J. Kamer, M. Beller and R. V. Jagadeesh, *Nat. Commun.*, 2018, **9**, 4123.
- 2 K. Murugesan, V. G. Chandrashekhar, T. Senthamarai, R. V. Jagadeesh and M. Beller, *Nat. Protoc.*, 2020, **15**, 1313–1337.
- 3 R. Kumar, N. J. Flodén, W. G. Whitehurst and M. J. Gaunt, *Nature*, 2020, **581**, 415–420.
- 4 G. M. Torres, Y. Liu and B. A. Arndtsen, *Science*, 2020, **368**, 318–323.
- 5 D. T. Smith, M. D. Delost, H. Qureshi, and J. T. Njardarson, Top 200 Pharmaceuticals by Retail Sales in 2020, <https://njardarson.lab.arizona.edu/sites/njardarson.lab.arizona.edu/files/Top%2020%20Pharmaceuticals%20by%20Retail%20Sales%202020V3.pdf>, accessed 16/04/2022.
- 6 S. Song, J. Qu, P. Han, M. J. Hülsey, G. Zhang, Y. Wang, S. Wang, D. Chen, J. Lu and N. Yan, *Nat. Commun.*, 2020, **11**, 4899.
- 7 Q. Hou, X. Qi, M. Zhen, H. Qian, Y. Nie, C. Bai, S. Zhang, X. Bai and M. Ju, *Green Chem.*, 2021, **23**, 119–231.
- 8 R. V. Jagadeesh, K. Murugesan, A. S. Alshammari, H. Neumann, M.-M. Pohl, J. Radnik and M. Beller, *Science*, 2017, **358**, 326–332.
- 9 O. I. Afanasyev, E. Kuchuk, D. L. Usanov and D. Chusov, *Chem. Rev.*, 2019, **119**, 11857–11911.
- 10 X.-P. Fu, P. Han, Y.-Z. Wang, S. Wang and N. Yan, *J. Catal.*, 2021, **399**, 121–131.
- 11 H. Qi, J. Yang, F. Liu, L. Zhang, J. Yang, X. Liu, L. Li, Y. Su, Y. Liu, R. Hao, A. Wang and T. Zhang, *Nat. Commun.*, 2021, **12**, 3295.
- 12 K. Alorku, C. Shen, Y. Li, Y. Xu, C. Wang and Q. Liu, *Green Chem.*, 2022, **24**, 4201–4236.
- 13 L. Lin, X. Han, B. Han and S. Yang, *Chem. Soc. Rev.*, 2021, **50**, 11270–11292.
- 14 N. S. Gould, H. Landfield, B. Dinkelacker, C. Brady, X. Yang and B. Xu, *ChemCatChem*, 2020, **12**, 2106–2115.
- 15 J. Han and J. Xie, *Chem*, 2020, **6**, 1053–1055.
- 16 T. Shen and T. H. Lambert, *J. Am. Chem. Soc.*, 2021, **143**, 8597–8602.
- 17 W. Deng, Y. Wang, S. Zhang, K. M. Gupta, M. J. Hülsey, H. Asakura, L. Liu, Y. Han, E. M. Karp, G. T. Beckham, P. J. Dyson, J. Jiang, T. Tanaka, Y. Wang and N. Yan, *Proc. Natl. Acad. Sci. U. S. A.*, 2018, **115**, 5093–5098.
- 18 T. Wang, J. Ibañez, K. Wang, L. Fang, M. Sabbe, C. Michel, S. Paul, M. Pera-Titus and P. Sautet, *Nat. Catal.*, 2019, **2**, 773–779.
- 19 C. Lin, J. Zhou, Z. Zheng and J. Chen, *J. Catal.*, 2022, **410**, 164–179.
- 20 J. G. Pereira, J. M. J. M. Ravasco, J. R. Vale, F. Queda and R. F. A. Gomes, *Green Chem.*, 2022, **24**, 7131–7136.
- 21 S. Song, V. Fung Kin Yuen, L. Di, Q. Sun, K. Zhou and N. Yan, *Angew. Chem., Int. Ed.*, 2020, **59**, 19846–19850.
- 22 S. Jiang, E. Muller, F. Jerome, M. Pera-Titus and K. D. O. Vigier, *Green Chem.*, 2020, **22**, 1832–1836.
- 23 M. Pelckmans, T. Renders, S. Van de Vyver and B. F. Sels, *Green Chem.*, 2017, **19**, 5303–5331.
- 24 P. V. Rathod, V. G. Deonikar, J. M. C. Puguán and H. Kim, *Fuel*, 2020, **264**, 116822.
- 25 M. Zhang, Y. Liu, B. Liu, Z. Chen, H. Xu and K. Yan, *ACS Catal.*, 2020, **10**, 5179–5189.
- 26 M. Yan, Y. Kawamata and P. S. Baran, *Chem. Rev.*, 2017, **117**, 13230–13319.
- 27 N. Saueremann, R. Mei and L. Ackermann, *Angew. Chem., Int. Ed.*, 2018, **57**, 5090–50947.
- 28 P. Su, W. Pei, X. Wang, Y. Ma, Q. Jiang, J. Liang, S. Zhou, J. Zhao, J. Liu and G. Q. Lu, *Angew. Chem., Int. Ed.*, 2021, **60**, 16044–16050.
- 29 H. Zou and J. Chen, *Appl. Catal., B*, 2022, **309**, 121262.
- 30 L. Du, L. Xing, G. Zhang, X. Liu, D. Rawach and S. Sun, *SusMat*, 2021, **1**, 150–173.
- 31 T. Gross, A. M. Seayad, M. Ahmad and M. Beller, *Org. Lett.*, 2002, **4**, 2055–2058.
- 32 Q. Yang, Y. Li, C. Ma, P. Fang, X. Zhang and T. Mei, *J. Am. Chem. Soc.*, 2017, **139**, 3293–3298.
- 33 J. J. Roylance and K.-S. Choi, *Green Chem.*, 2016, **18**, 5412–5417.
- 34 Z. Zheng, L. Yu, M. Gao, X. Chen, W. Zhou, C. Ma, L. Wu, J. Zhu, X. Meng, J. Hu, Y. Tu, S. Wu, J. Mao, Z. Tian and D. Deng, *Nat. Commun.*, 2020, **11**, 3315.
- 35 M. Wu, G. Zhang, H. Tong, X. Liu, L. Du, N. Chen, J. Wang, T. Sun, T. Regier and S. Sun, *Nano Energy*, 2021, **79**, 105409.
- 36 Q. Fu, J. Han, X. Wang, P. Xu, T. Yao, J. Zhong, W. Zhong, S. Liu, T. Gao, Z. Zhang, L. Xu and B. Song, *Adv. Mater.*, 2021, **33**, 1907818.
- 37 M. Zhang, Y. He, D. Yan, H. Xu, A. Wang, Z. Chen, S. Wang, H. Luo and K. Yan, *Nanoscale*, 2019, **11**, 22255–22260.
- 38 J. Zhang, J. Wu, H. Guo, W. Chen, J. Yuan, U. Martinez, G. Gupta, A. Mohite, P. M. Ajayan and J. Lou, *Adv. Mater.*, 2017, **29**, 1701955.
- 39 J. Lu, F. Lian, Y. Zhang, N. Chen, Y. Li, F. Ding and X. Liu, *J. Mater. Chem. A*, 2020, **8**, 6532–6538.
- 40 Y. Wang, Z. Zhang, Y. Mao and X. Wang, *Energy Environ. Sci.*, 2020, **13**, 3993–4016.
- 41 Y. Takahashi, Y. Kobayashi, Z. Wang, Y. Ito, M. Ota, H. Ida, A. Kumatani, K. Miyazawa, T. Fujita, H. Shiku, Y. E. Korchev, Y. Miyata, T. Fukuma, M. Chen and T. Matsue, *Angew. Chem., Int. Ed.*, 2020, **59**, 3601–3608.
- 42 T. Lei, M. Xianguang, D. Dehui and B. Xinhe, *Adv. Mater.*, 2019, **31**, 1901996.
- 43 Z. Chen, G. Zhang, H. Chen, J. Prakash, Y. Zheng and S. Sun, *Renewable Sustainable Energy Rev.*, 2022, **155**, 111922.
- 44 Y. Liu, J. Wu, K. P. Hackenberg, J. Zhang, Y. M. Wang, Y. Yang, K. Keyshar, J. Gu, T. Ogitsu, R. Vajtai, J. Lou, P. M. Ajayan, B. C. Wood and B. I. Yakobson, *Nat. Energy*, 2017, **2**, 17127.

- 45 G. M. Carroll, H. Zhang, J. R. Dunklin, E. M. Miller, N. R. Neale and J. van de Lagemaat, *Energy Environ. Sci.*, 2019, 12, 1648–1656.
- 46 X. Meng, C. Ma, L. Jiang, R. Si, X. Meng, Y. Tu, L. Yu, X. Bao and D. Deng, *Angew. Chem., Int. Ed.*, 2020, 59, 10502–10507.
- 47 K. L. Zhou, C. B. Han, Z. Wang, X. Ke, C. Wang, Y. Jin, Q. Zhang, J. Liu, H. Wang and H. Yan, *Adv. Sci.*, 2021, 8, 2100347.
- 48 L. Wang, J. Zou, S. Chen, G. Zhou, J. Bai, P. Gao, Y. Wang, X. Yu, J. Li, Y.-S. Hu and H. Li, *Energy Storage Mater.*, 2018, 12, 216–222.
- 49 X. Lu, K. Xu, S. Tao, Z. Shao, X. Peng, W. Bi, P. Chen, H. Ding, W. Chu, C. Wu and Y. Xie, *Chem. Sci.*, 2016, 7, 1462–1467.
- 50 H. Tao, M. Zhou, R. Wang, K. Wang, S. Cheng and K. Jiang, *Adv. Sci.*, 2018, 5, 1801021.
- 51 X. Huang, J. Tang, B. Luo, R. Knibbe, T. Lin, H. Hu, M. Rana, Y. Hu, X. Zhu, Q. Gu, D. Wang and L. Wang, *Adv. Energy Mater.*, 2019, 9, 1901872.
- 52 P. C. Sherrell, K. Sharda, C. Grotta, J. Ranalli, M. S. Sokolikova, F. M. Pesci, P. Palczynski, V. L. Bemmer and C. Mattevi, *ACS Omega*, 2018, 3, 8655–8662.
- 53 G. A. Tritsarlis, E. Kaxiras, S. Meng and E. Wang, *Nano Lett.*, 2013, 13, 2258–2263.
- 54 M. Inoue, H. P. Hughes and A. D. Yoffe, *Adv. Phys.*, 1989, 38, 565–604.
- 55 A. Maiti and S. K. Srivastava, *J. Mater. Chem. A*, 2018, 6, 19712–19726.
- 56 T. Liu, N. Peng, X. Zhang, R. Zheng, M. Xia, H. Yu, M. Shui, Y. Xie and J. Shu, *Nano Energy*, 2021, 79, 105460.
- 57 J. Tang, X. Huang, T. Lin, T. Qiu, H. Huang, X. Zhu, Q. Gu, B. Luo and L. Wang, *Energy Storage Mater.*, 2020, 26, 550–559.
- 58 C. W. Lin, X. J. Zhu, J. Feng, C. Z. Wu, S. L. Hu, J. Peng, Y. Q. Guo, L. L. Peng, J. Y. Zhao, J. L. Huang, J. L. Yang and Y. Xie, *J. Am. Chem. Soc.*, 2013, 135, 5144–5151.
- 59 Z. Hu, Z. Tai, Q. Liu, S.-W. Wang, H. Jin, S. Wang, W. Lai, M. Chen, L. Li, L. Chen, Z. Tao and S.-L. Chou, *Adv. Energy Mater.*, 2019, 9, 201803210.
- 60 O. Kikhtyanin, V. Korolova, A. Spencer, L. Dubnová, B. Shumeiko and D. Kubička, *Catal. Today*, 2021, 367, 248–257.
- 61 Y. Wang, S. Furukawa, Z. Zhang, L. Torrente-Murciano, S. A. Khan and N. Yan, *Catal. Sci. Technol.*, 2019, 9, 86–96.
- 62 K. Kaiden, T. Matsui and S. Tanaka, *Appl. Spectrosc.*, 1987, 41, 180–184.
- 63 L. Luo, Z. Wang, X. Xiang, D. Yan and J. Ye, *ACS Catal.*, 2020, 10, 4906–4913.
- 64 H. Liu, W. Jia, X. Yu, X. Tang, X. Zeng, Y. Sun, T. Lei, H. Fang, T. Li and L. Lin, *ACS Catal.*, 2021, 11, 7828–7844.
- 65 M. S. Rozenberg, T. Nishio and T. Steiner, *New J. Chem.*, 1999, 23, 585–586.
- 66 A. Mielcarek and A. Dołęga, *J. Mol. Struct.*, 2016, 1103, 217–223.
- 67 B. Ravel and M. Newville, *J. Synchrotron Radiat.*, 2005, 12, 537–541.